Journal of Materials Chemistry A

ROYAL SOCIETY OF CHEMISTRY

PAPER

View Article Online
View Journal | View Issue



Cite this: J. Mater. Chem. A, 2026, 14, 19784

# Developing a series of calcium-doped pyrochlore iridates for the oxygen evolution reaction in PEM water electrolysis

Felix Kerner, [a] Kohei Miyazaki [bc] and Daniel Schröder *[ad]

Received 5th November 2025
Accepted 10th April 2026

DOI: 10.1039/d5ta08986g

rsc.li/materials-a

Active and stable catalysts for the oxygen evolution reaction (OER) with reduced precious metal content are crucial for green hydrogen production. State-of-the-art OER catalysts used in proton exchange membrane water electrolysis (PEMWE) like ruthenium oxides and iridium oxides either show insufficient stability in the acidic environment or exhibit high cost due to their high iridium-content. In recent studies, iridium-containing pyrochlores ($A_2Ir_2O_7$) gained interest as possible OER catalysts for PEMWE, due to their high activity at reduced iridium content compared to $IrO_2$. Although several doping strategies were found to boost the OER properties of the pyrochlore ruthenates even further, few studies have focused on the iridates, yet. While doping degrees were limited to one specific composition in the iridate case so far, we herein we present a series of six praseodymium iridates ($Pr_2Ir_2O_7$) where we systematically replaced A-site $Pr^{3+}$ with $Ca^{2+}$. Electrochemical measurements with a rotating disk electrode (RDE) demonstrate that the Ca-doping has a positive effect on the mass activity of the material. Simultaneously, iridium dissolution, evidenced by inductively coupled plasma mass spectrometry (ICP-MS), is significantly reduced by the doping. We report an up to 100% increase in the stability number (*S*-number) when compared to the undoped catalyst. This work presents a promising perspective to further enhance pyrochlore iridates as efficient OER catalysts for water splitting.



## Introduction

Proton exchange membrane (PEM) electrolysis has established itself as the most promising and effective technology for the production of green hydrogen. It combines capability of high power and (differential) pressure, compact design, and fast adaptability to variable power inputs, as well as high hydrogen purity and high energy efficiency.[1,2] However, the sluggish kinetics of the anodic oxygen evolution reaction (OER), the trade-off between activity and stability of OER catalysts, as well as their high cost are still relevant aspects that leave room for further improvement of PEM water electrolyzers (PEMWEs). In commercial applications iridium-based materials have emerged as the most advanced and reliable catalysts. Although ruthenium oxides show higher activity, iridium oxides show a good compromise between moderate activity and high stability under acidic conditions.[3] However, due to iridium being one of the rarest elements on earth only mined as a byproduct of platinum and palladium production, and the high prices associated with this, it could become the bottleneck of a mature market.[4] Therefore, the development of novel catalytic systems with reduced iridium content and increased intrinsic activity remains a critical task in PEMWE research.[5,6] In recent years, perovskite ($AIrO_3$) and pyrochlore ($A_2Ir_2O_7$) iridium oxide materials have drawn considerable attention, due to their high specific OER activities at reduced noble metal content, facilitating lowered cost compared to state of the art ruthenium or iridium oxides.[5–9] One of the most prominent perovskites for acidic OER is $SrIrO_3$, which showed superior activity compared to ruthenium oxide and iridium oxide systems.[7] It was even found that the activity of $SrIrO_3$ increases further as the measurement progresses, which was hypothesized originating from leakage of the A-site Sr into the electrolyte solution and the simultaneous surface reconstruction and surface roughening.[7,10] For the pyrochlore iridates there is a vast amount of examples in the literature: Lebedev *et al.* synthesized pyrochlore iridates with yttrium, bismuth, lead as well as with mixtures of them in the A-site. Especially the yttrium- and bismuth-iridates were found to have promising activities surpassing the activity of $IrO_2$ with similar surface area. Similar to $SrIrO_3$, the authors hypothesized that the high intrinsic activity, which increased even further in the course of the measurements originates from A-site ion leakage and formation of a highly active $IrO_x$ surface layer. Overall, Lebedev *et al.* concluded, that catalysts with

[a]Technische Universität Braunschweig, Institute of Energy and Process Systems Engineering (InES), Langer Kamp 19B, 38106 Braunschweig, Germany. E-mail: d.schroeder@tu-braunschweig.de
[b]Kyoto University, Graduate School of Engineering, Kyoto 615-8510, Japan
[c]Kobe University, Graduate School of Engineering, Kobe 657-8501, Japan
[d]Technische Universität Braunschweig, Battery LabFactory Braunschweig (BLB), Langer Kamp 19, 38106 Braunschweig, Germany

pyrochlore structure improve the specific activity of iridium-based catalysts and offer the possibility to develop low cost, active and stable anodes for PEMWE.[6] Shih *et al.* found a similar but even slightly higher mass activity for a single-phase $Y_2Ir_2O_7$ material.[5] Kim *et al.* synthesized the ruthenate analogue and also found that the pyrochlore catalyst $Y_2Ru_2O_7$ exhibits increased activity compared to the $RuO_2$ material.[11] Shang *et al.* investigated the influence of a series of rare earth metals as the A-site ions on the OER performance of pyrochlore iridates (A = Ho, Tb, Gd, Nd, Pr). They found that the activity increases within the series with higher ionic radii of A, resulting in $Pr_2Ir_2O_7$ being the most active representative of the series. The authors attributed this finding to an insulator–metal transition going from A = Ho to Pr caused by weakening of electron correlations, which led to a more covalent metal–oxygen bond in the case of the higher ionic radius $Pr^{3+}$.[12]

Building on these findings, there were attempts to tune the electronic properties of pyrochlore iridates and ruthenates even further by doping heteroatoms into the lattice: Feng *et al.* were the first group who synthesized a A-site doped yttrium ruthenate pyrochlore by the partial replacement of $Y^{3+}$ with $Zn^{2+}$. They found that the doping significantly improves the activity of the catalyst and proposed that the A-site doping strategy may also be suitable for other pyrochlore ruthenates and pyrochlore iridates.[13] Feng *et al.* then went one step further and synthesized three series of OER catalysts $Y_{2-x}M_xRu_2O_7$ (with M = Mg, Ca and Ba), each with 4–5 doping ratios. For each series they found an optimum ratio, showing the highest OER performances: $Y_{1.85}Mg_{0.15}Ru_2O_7$, $Y_{1.75}Ca_{0.25}Ru_2O_7$, $Y_{1.85}Ba_{0.15}Ru_2O_7$.[14–16] Kuznetsov *et al.* varied the A-site metal in $Y_{1.8}M_{0.2}Ru_2O_7$ (with M = Fe, Co, Ni and Cu) at a fixed ratio and found the copper analogue being the most active of the series.[17] Besides these metal doping strategies, there are also two studies on anion doping of the same base material: Wang *et al.* synthesized a series of F-doped $Y_2Ru_2O_7$ while Yang *et al.* synthesized a series of the S-doped analogues. Both groups found enhanced activities compared to the base compound and an optimum doping ratio.[18,19] In contrast to the extensive research on pyrochlore ruthenates, little work has been done on doping of pyrochlore iridates for the application as OER catalysts. To the best of our knowledge, the only example is by Zhu *et al.* who developed two pyrochlore materials $M_{1.8}Zn_{0.2}Ir_2O_7$ in which the trivalent rare-earth metal A-site ions $Pr^{3+}$ and $Lu^{3+}$ were partially replaced by the bivalent transition metal ion $Zn^{2+}$. The two Zn-doped materials both showed superior catalytic activity as well as a higher stability compared to the undoped materials.[20] All of those strategies have one thing in common: the authors rationalized, that the heteroatom doping leads to an increase in the covalency of the Ru–O/Ir–O bond and/or the introduction of oxygen vacancies into the lattice.[13–20] Both effects are beneficial for the OER performance since they promote the lattice oxygen mechanism (LOM), one of the two concurring mechanisms of the OER shown in Scheme 1.[18,21] Our work aims to build on these advantages and to improve the activity of this novel material group even further. While prior work on the doping of pyrochlore iridates was restricted to only one specific ratio ($M_{1.8}Zn_{0.2}Ir_2O_7$), broad systematic series of doped pyrochlore

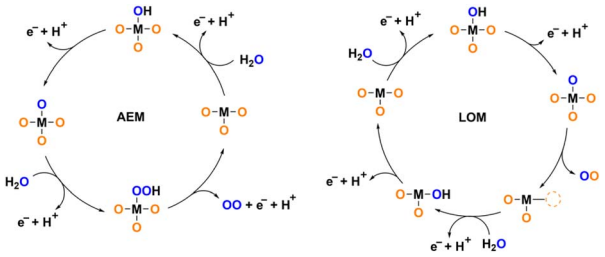


Scheme 1 OER mechanisms in acidic media: adsorbate evolution mechanism (AEM) and lattice oxygen mechanism (LOM). Orange oxygen atoms represent lattice oxygen, blue oxygen atoms represent atoms from the electrolyte, oxygen vacancies are shown as dashed circles. Adapted from Shan *et al.*[21]

ruthenates showed, that it is crucial to explore a series of doping degrees to find the optimal OER catalyst.[14–16,20] In this work, we aimed to broaden the scope and explore the limits of the dopant content in the pyrochlore iridate structure as well as the influence of increasing dopant content on the catalytic performance and stability of the materials. By partially replacing trivalent $Pr^{3+}$ with lower charge but similar ionic radius $Ca^{2+}$, our goal was to alter the electronic structure/environment of iridium resulting in higher covalency of the Ir–O bond and the introduction of oxygen vacancies and by this in the enhancement of the material's catalytic activity. While there was already an attempt of systematic doping of calcium into the lattice of $Pr_2Ir_2O_7$ reported by Converse, their scope was significantly different from ours. The authors applied a solid-state synthesis route, were they found impurities already at $x > 0.2$ and they focused on determining the materials' structural, electrical and magnetic properties.[22] However, the materials application as OER catalysts was not investigated. In the present work, with the aim of extending the view on this material class, we synthesized a series of $Pr_2Ir_2O_7$ with six different doping ratios, using a milder hydrothermal synthesis method, structurally characterized them and probed their possible application as OER catalysts in PEM acidic water electrolysis, finally closing this gap. Moreover, we not only investigate the impact of varying doping degrees on the material's activity, but also their efficiency, determined by the stability number (*S*-number), an efficiency metric initially introduced by Geiger *et al.*[23] *S*-Numbers have not been investigated in the context of pyrochlore iridates, yet. Therefore, our approach of systematic doping and evaluation of the respective *S*-numbers offers valuable insights for future directions.

# Experimental

## Materials and synthesis

Six pyrochlore $Pr_{2-x}Ca_xIr_2O_{7-\delta}$ powders with $x = 0$, 0.1, 0.2, 0.3, 0.4, and 0.5 were synthesized using a hydrothermal synthesis method. Iridium(IV) chloride ($IrCl_4$), praseodymium(III) nitrate hexahydrate ($Pr(NO_3)_3 \cdot 6H_2O$) and calcium nitrate tetrahydrate ($Ca(NO_3)_2 \cdot 4H_2O$) were each dissolved in DI water in separate containers to obtain stock solutions containing 0.1 mol $L^{-1}$ of the respective metal. Sodium hydroxide was dissolved in DI

water in a fourth container with a final concentration of 1.0 mol $L^{-1}$. 10 mL of the iridium-containing solution was added to a hydrothermal reactor made from PTFE. To obtain the calcium-doped catalysts ($x = 0$, 0.1, 0.2, 0.3, 0.4, 0.5), the stoichiometric amounts of the praseodymium- and calcium-containing solutions were added with respect to iridium. 20 mL of the NaOH solution was added, followed by a waiting time of 5 min. Finally, the mixture was complemented by DI water to give a final volume of 53.5 mL before the hydrothermal reactor was closed with a PTFE lid and placed in a stainless-steel container (HU-100). The mixture was reacted in an oven at 200 °C for 12 h. The black powder was filtered off and washed five times using DI water before it was dried under air atmosphere at 60 °C for 24 h. After drying, the black solid was ground using an agate mortar and pestle, before it was transferred to a melting pot and calcinated in air at 600 °C for 12 h. In the end, a fine black powder was obtained. For the following, the materials $Pr_{2-x}Ca_xIr_2O_{7-\delta}$ are labeled as PCIO-$x$ with $x$ representing the respective Ca-content.

### Structural characterization

Powder X-ray diffraction (XRD) was measured using a Rigaku SmartLab with Cu Kα radiation ($\lambda = 1.5406$ Å), voltage 40 kV, current 30 mA, step size 0.01°, $2\theta$ from 10° to 90°. The specific surface area was determined by measuring nitrogen adsorption at 77 K using a BEL Japan Inc., Belsorp-mini II. Before the measurement, the samples were degassed under vacuum at 120 °C for 3 h. The Brunauer–Emmett–Teller (BET) surface area was determined by evaluating the adsorption isotherms in the $p/p_0$ range of 0.05–0.30. The elemental composition of the catalyst materials was determined by measuring X-ray fluorescence (XRF) using a Malvern Panalytical Epsilon 1. Scanning electron microscopy (SEM) pictures were taken using a Thermo Fisher Scientific Helios G4 CX with an acceleration voltage of 5 kV and a current of 10 nA. Prior to the measurement, the samples were coated with 4.2 nm platinum using a Leika EM ACE200 sputter coater. SEM energy dispersive X-ray spectroscopy (SEM-EDX) mapping was carried out using a JEOL JSM-IT800HL equipped with a DrySD EDS detector. X-ray photoelectron spectroscopy (XPS) was measured using a Shimadzu Co. ESCA-3400 equipped with a Mg Kα source (1253.6 eV). The XPS data was evaluated using CasaXPS software. All high-resolution spectra were calibrated to the C 1s peak of adventitious carbon shifted to 284.8 eV.

### Electrochemical characterization

Catalyst ink was prepared by dispersing 5.0 mg of catalyst, 1.0 mg of Vulcan XC72R in a mixture of 750 μL DI water and 250 μL isopropanol before adding 21.5 μL Nafion solution (5 wt%, D521, Ion Power) as a binder. The ink was shaken, sonicated with an ultrasonic horn, shaken again and sonicated in an ice bath for 30 min. The ink was sonicated in an ultrasonic bath for 5 min and shaken again right before 10 μL were drop-casted in one portion onto a mirror-polished Au RDE tip ($\Phi$ 5 mm), which was then dried under air atmosphere at 60 °C for 30 min. The electrochemical tests were conducted in a three-electrode configuration using a Low Volume RDE Cell (PINE) with a graphite rod counter electrode, an Ag/AgCl 3 M KCl reference electrode, the catalyst-coated RDE as the working electrode as well as 9.0 mL of 0.1 M $HClO_4$ as the electrolyte. The measurement was controlled by a SP240 potentiostat (Biologic). Before the measurement was started, humidified $O_2$ gas was bubbled through the electrolyte for 30 min, with the WE set to a rotation rate of 1600 rpm. During the measurement, the $O_2$ stream was flown over the electrolyte solution while the rotation rate of the RDE was kept at 1600 rpm. First, 10 cycles of cyclic voltammetry (CV) were measured from 0.8 V to 1.5 V *vs.* Ag/AgCl 3 M KCl with a scan rate of 20 mV $s^{-1}$ to evaluate the OER performance of the catalysts. For the evaluation of the CV experiments the currents of forward and reverse scans of the 10th CV cycle were averaged. Next, with the aim of estimating the electrochemically active surface area (ECSA) from the double layer capacity, CV was measured between 0.8 V and 1.0 V at scan rates of 10, 20, 50, 75, 100, 150, and 200 mV $s^{-1}$. After this, a galvanostatic impedance spectroscopy (GEIS) measurement was performed at 10 mA $cm_{geo}^{-2}$ with an AC amplitude of 0.05 μA $cm_{geo}^{-2}$ (5% of DC current) to determine the ohmic resistance of the solution for *iR*-correction from the high frequency resistance (HFR). The measured values for $R$ were ~23 Ω for all measurements. At the end of the measurement, a stability test was performed by applying chronopotentiometry (CP) with a current of 10 mA $cm_{geo}^{-2}$ for 1 h. After the measurement was finished, a sample of 5 mL electrolyte was taken for the ICP-MS analysis to determine the amount of dissolved iridium. Regardless of the PCIO material in use, the catalyst inks behaved equally and the catalyst films were similar in appearance. To account for random deviations in film homogeneity and roughness, the RDE measurement was repeated three times for each catalyst material, and the average values and standard deviation are displayed in the figures below. Additionally, one measurement was conducted with a layer consisting only of Vulcan XC72R and binder, but without catalyst, which was used as a blank for correction for the CV measurements and for onset potential definition. The onset potential was defined as ten times the current of the blank measurement. Carbon corrosion was assumed to be negligible under the described measurement conditions and the short total measurement time (<2 h). All potentials were referenced to the potential of the reversible hydrogen electrode (RHE). For this, the potential of the Ag/AgCl reference electrode was measured *versus* an RHE (HydroFlex, Gaskatel) in the electrolyte solution. Additionally, the pH of the electrolyte was determined using a freshly calibrated Mettler Toledo InLab Routine Pro pH electrode. The pH of the electrolyte solution was determined to be 1.04. The potential of the Ag/AgCl reference electrode *versus* the RHE was 266 mV, which is close to the theoretical value at this pH (268.4 mV).

### Inductively-coupled plasma mass spectrometry

To quantify the amount of iridium dissolved into the electrolyte during the measurements, samples were taken from the Low Volume Cell after the RDE measurements (CV, ECSA

 

determination, GEIS and CP) were finished. The samples were then analyzed using an ICP-MS (PlasmaQuant MS Q, Analytik Jena). The device was calibrated using nine different standard solutions (0, 0.1, 0.25, 0.50, 0.75, 1.0, 2.0, 3.0, 5.0 μg $L^{-1}$), with each one also containing 20 μg $L^{-1}$ of $^{89}Y$ as an internal standard to account for possible matrix effects. The standards were prepared from a single element Ir standard (Supelco Certipur® Iridium ICP Standard 1000 mg $L^{-1}$ Ir), a single element Y standard (Supelco Certipur® Yttrium ICP Standard 1000 mg $L^{-1}$ Y) and a 2–3% nitric acid solution (Supelco Suprapur® Nitric acid 65%, diluted using Milli-Q water to give 2–3% $HNO_3$). The samples taken from the RDE measurements were diluted 1 : 10 with 2–3% $HNO_3$ before being measured with the ICP-MS. These samples also contained the internal standard $^{89}Y$ in a concentration of 20 μg $L^{-1}$. The measurements were conducted without gas as well as in KED mode with helium in the integrated collision reaction cell (iCRC), both in peak hopping mode (1 point per peak, 12 scans per repetition, 5 repetitions per sample). For the analysis, the signal of $^{193}Ir$ in the helium mode was used.

## Results and discussion

### Structural characterization

The XRD patterns in Fig. 1a show for $x = 0$ to 0.4 only one phase with all reflexes assignable to the cubic phase ($Fd\bar{3}m$) of the base structure $Pr_2Ir_2O_7$ (ICSD: 156436). This finding indicates that calcium can successfully be incorporated into the pyrochlore lattice, where it partially replaces praseodymium. In the case of PCIO-0.5, at least one additional phase next to the pyrochlore phase is visible. Several reflexes can be assigned to $IrO_2$ (ICSD: 81028), which suggests that the solution limit of $Ca^{2+}$ in the $Pr^{3+}$ lattice is reached somewhere between $x = 0.4$ and 0.5, and the excess iridium crystallizes as $IrO_2$. The excess calcium should most likely be removed from the solution during the washing steps. However, there are still additional low intensity reflexes at $2\theta = 18.7°$, 32.7° and 33.7° which can most likely be assigned to some small impurity of $Ca_2IrO_4$ or $CaIrO_3$ perovskites.[24] We hypothesize that the solution limit of calcium in the pyrochlore structure led to an excess of $Ca^{2+}$ and $Ir^{4+}$ in the solution, which then form the impurities. Since the ionic radii of $Ca^{2+}$ (1.12 Å) and $Pr^{3+}$ (1.13 Å) in eight-fold cubic coordination are almost even, only a slight decrease in the lattice parameter going from $x = 0$ to $x = 0.5$ is expected.[25] To prove this, the XRD patterns were refined using CELREF Version 3 and the reflexes indicated as 1–9 in Fig. 1a for PCIO-0.0 to PCIO-0.4. Due to the iridium oxide impurity in PCIO-0.5, the reflexes that are influenced by the impurity need to be neglected, leaving reflexes 1, 3, 5, 6, and 8 for determination of the lattice parameter *a*. Fig. 1b shows lattice parameter *a* after unit cell refinement plotted *versus* the calcium content. The lattice constant *a* slightly decreases from 10.369 Å ($x = 0.0$) to 10.343 Å ($x = 0.5$). The almost perfectly linear trend of decreasing lattice parameter with increasing doping degree shows that the partial exchange of $Pr^{3+}$ by the slightly smaller $Ca^{2+}$ indeed leads to a slight contraction of the lattice. To further prove the successful incorporation of calcium

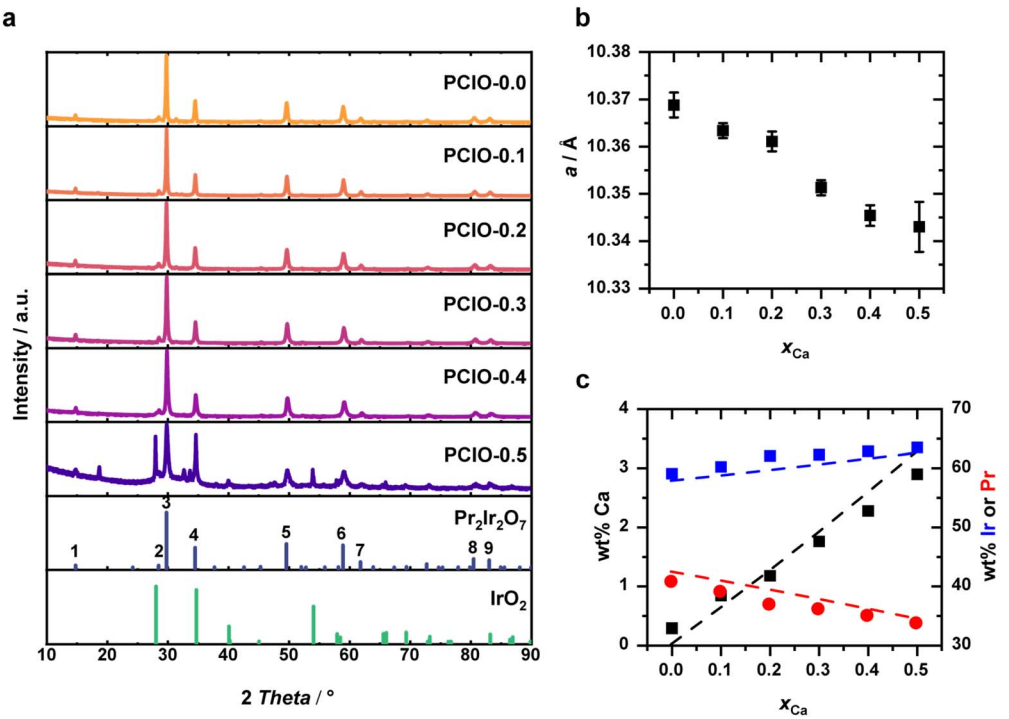


Fig. 1 Results derived from X-ray diffraction measurements of the as-received powder samples after calcination: (a) diffraction pattern of PCIOs and reference data of $Pr_2Ir_2O_7$ (ICSD: 156436) and $IrO_2$ (ICSD: 81028), (b) variation of lattice constant *a* with Ca-content derived from unit cell refinement (points), (c) variation of metal weight percentages of iridium, praseodymium and calcium derived from XRF measurements (points) as well as trend lines calculated from the theoretical composition (dashed lines).

into the lattice, XRF analysis was performed. The measured weight percentages of the three metals were normalized to their sum and the resulting semi-quantitative weight percentages are plotted *versus* the calcium content in Fig. 1c. Additionally, as a reference, the theoretical weight percentages were calculated from the ideal compositions and the theoretical trends are plotted as well as dashed lines. The normalization and the calculations for the theoretical weight percentages are described in detail in the SI. With increasing calcium-doping there is a slight decrease in the praseodymium content, while the calcium content is slightly increasing. This behavior is somehow expected, since calcium partially replaces praseodymium in the structure. Furthermore, the iridium content is slightly increasing with increasing doping degree, since the molar mass of the PCIO is slightly reduced when praseodymium ($M = 140.91$ g mol$^{-1}$) is substituted by lower mass calcium ($M =$ 40.08 g mol$^{-1}$). Although there are some small offsets, the overall trends in the compositions are in good agreement with the theoretical mass percentages calculated from the theoretical compositions. Together with the findings from the XRD analysis, it is confirmed that praseodymium was indeed partially replaced by calcium up to a content between $x = 0.4$ and 0.5. In the case of PCIO-0.5, the exchange limit seems to be reached, and a mixture of PCIO and $IrO_2$ with some minor impurities is formed. With the chemical composition of the materials confirmed, the catalysts morphology was investigated. For this the mean crystallite size of the catalyst particles was determined by analyzing the peak broadening of the reflexes 5–7 and applying Scherrer's eqn (1). Where $\tau$ is the crystallite size, $K$ is Scherrer's constant with a value of 0.90, $\lambda$ is the wavelength of the X-rays (0.15406 nm), $\beta$ and $\theta$ are the FWHM and the Bragg angle of the respective peak.

$$\tau = \frac{K\lambda}{\beta \cos(\theta)} \quad (1)$$

Fig. 2a shows the mean crystallite size determined from Scherrer's equation *versus* the calcium content for all samples testes. The crystallite size decreases from PCIO-0.0 to PCIO-0.5. This decrease in crystallite size should, in theory, lead to an increase in surface area for the electrochemical testing. The increase of the physically available surface is supported by the nitrogen adsorption experiments: with increasing calcium-content, a trend towards higher BET surface areas is observed as illustrated in Fig. 2b. The adsorption isotherms as well as the BET analysis are shown in the SI (Fig. S1).

To gain further insights into the morphology of the catalyst particles, SEM images where taken. The SEM images of PCIO-0.0 and PCIO-0.5 are shown in Fig. 2c–e. They show submicron particle agglomerates. The agglomeration of PCIO-0.0 (Fig. 2c) shows particles with a broad range of sizes mostly in the range of 100–300 nm. In the case of PCIO-0.5 (Fig. 2d) more of a tree-like agglomeration is obtained where separate particles can hardly be discriminated. However, they appear to be at least four times smaller in size. This finding further strengthens the findings from the Scherrer analysis and BET analysis. With

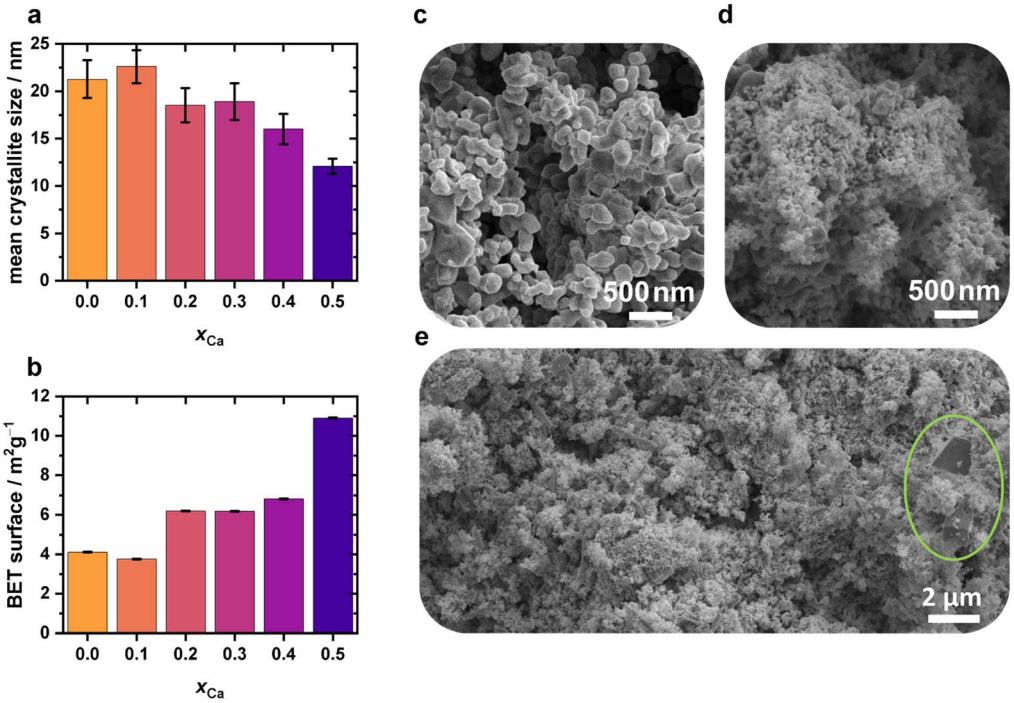


Fig. 2 Results from morphology analysis: (a) mean crystallite size derived from XRD analysis by Scherrer's equation and (b) specific surface areas determined from $N_2$ adsorption measurements and BET analysis. SEM images of PCIO-0.0 and PCIO-0.5: (c) agglomeration of PCIO-0.0 particles, (d) tree-like agglomeration of PCIO-0.5 particles; (e) lower magnification picture of PCIO-0.5 with larger impurity particle (green circle, likely $IrO_2$).

 

decreasing crystallite and particle size the specific surface area increases, theoretically increasing the area available for OER. When looking at a lower magnification of the SEM images some larger particles from another phase are visible for PCIO-0.5 (Fig. 2e). Since the XRD reflexes of the $IrO_2$ impurity in the diffraction pattern of PCIO-0.5 are significantly sharper than the reflexes assigned to the $Pr_2Ir_2O_7$ structure, suggesting a higher crystallite size according to Scherrer's equation, these larger particles in the SEM picture can likely be assigned to the $IrO_2$ impurity. However, the majority of the particles still has the tree-like morphology of the PCIO material, suggesting a relatively low fraction of impurities in this analyzed sample. SEM images of all six samples are shown in the SI (Fig. S2). SEM-EDX mapping (shown in the SI, Fig. S3) revealed a homogeneous distribution of O, Ca, Pr, and Ir in all PCIO materials. Moreover, the increasing relative Ca Kα signal intensity with higher doping levels is consistent with the compositional trends observed by XRF before.

XPS was measured to investigate the effect of the calcium doping on the surface composition of the materials. Fig. 3a shows the spectra of the O 1s region. The spectra were corrected by the integral background and fitted with two peaks. In agreement with the literature, these peaks were assigned to surface lattice oxygen ($O_{lat}$) at ~529.1 eV and adsorbed oxygen at ~531.3 eV ($O_{ads}$), with the latter representing a variety of different oxygen species including surface hydroxyls and other (adsorbed) oxygen species (*e.g.* $O^{2-}$, $O_2^{2-}$, $O^-$, $OH^-$).[13,26] Signals in the same binding energy region as $O_{ads}$ have also frequently been assigned to oxygen species indicative of oxygen vacancies.[17,27] With increasing calcium content, the share of $O_{ads}$ increases linearly from 72.6% to 82.1%, while that of $O_{lat}$ decreases, as shown in Fig. 3b. The spectra of the Ir 4f region (depicted in the SI, Fig. S4) show no significant change in line shape, indicating that iridium remains predominantly unchanged in the $Ir^{4+}$ state upon calcium doping. Higher concentrations of oxygen vacancies and hydroxyl species, have both previously been correlated with enhanced OER activity.[13–17,28–30] Surface hydroxyl groups have been assumed to act as reactive surface intermediates on active sites, while oxygen vacancies have been considered as adsorption sites for intermediates.[14–16,30] Both occur in the LOM shown in Scheme 1. Therefore, we propose, that the necessary charge compensation, due to the exchange of $Pr^{3+}$ with the lower-charge $Ca^{2+}$ proceeds *via* the formation of additional active surface hydroxyls and/or additional oxygen vacancies.

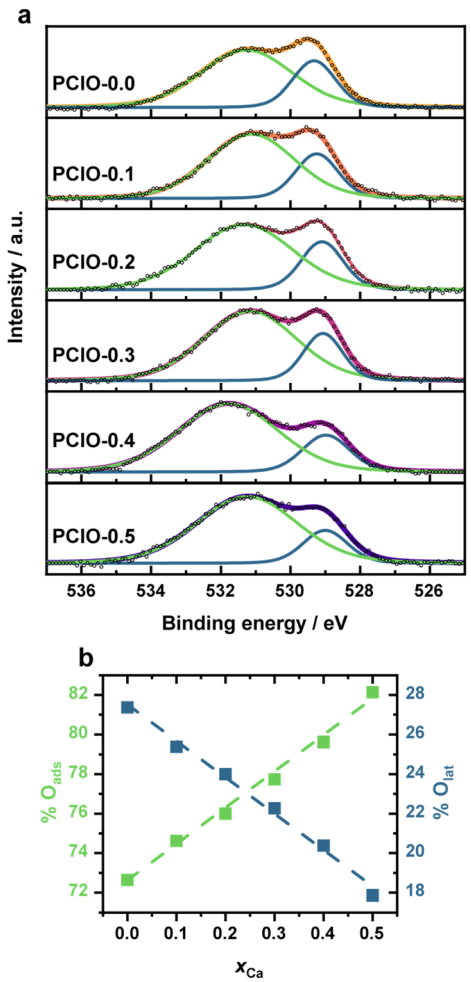


Fig. 3 O 1s XPS spectra (a) and peak area shares of $O_{lat}$ and $O_{ads}$ (b).

## Electrochemical activity and stability

Since iridium provides the active sites for the OER and is also the most expensive element in the catalysts, the measured current was normalized to the mass of iridium present in the catalyst layer of the RDE. The mass activity plots in Fig. 4a and b show that the activity increases with increasing Ca-content in the PCIO series. However, the increase in activity becomes most pronounced with PCIO-0.4 and PCIO-0.5. The onset potentials of the six PCIO materials are shown in Fig. 4c. While PCIO-0.0 to PCIO-0.3 exhibit similar onset potentials in the range of 1.500–1.505 V *vs.* RHE, the two materials with higher calcium content exhibit lower onset potentials of 1.483 V (PCIO-0.4) and 1.472 V (PCIO-0.5), again indicating a better activity for those materials. By performing CV measurements at different scan rates in the non-faradaic region the electrochemically active surface area (ECSA) of the PCIO materials was estimated (Fig. 4d). A detailed explanation of the ECSA determination as well as the respective CVs can be found in the SI (Fig. S5–S10). Similar to the findings of the BET and SEM analysis, the ECSA is increasing when the Ca-content is increased. The Ca-doping appears to make the catalysts form in smaller particle size leading to an enlarged electrochemically accessible interface and by this higher number of active sites accessible for the OER to take place. This likely results in reduced local current densities at the electrode/electrolyte interface possibly leading to increased durability of the material. The activity of the catalysts was also evaluated in a Tafel plot (Fig. 4e). While undoped PCIO and PCIO-0.1 exhibit similar, rather high Tafel slopes of ~50 mV $dec^{-1}$, higher doping levels show a positive influence on the Tafel slope, reaching a value of 43.8 mV $dec^{-1}$ with PCIO-0.5. In order to investigate, if the increased activity of the PCIOs with high calcium content solely originates from increased surface area or

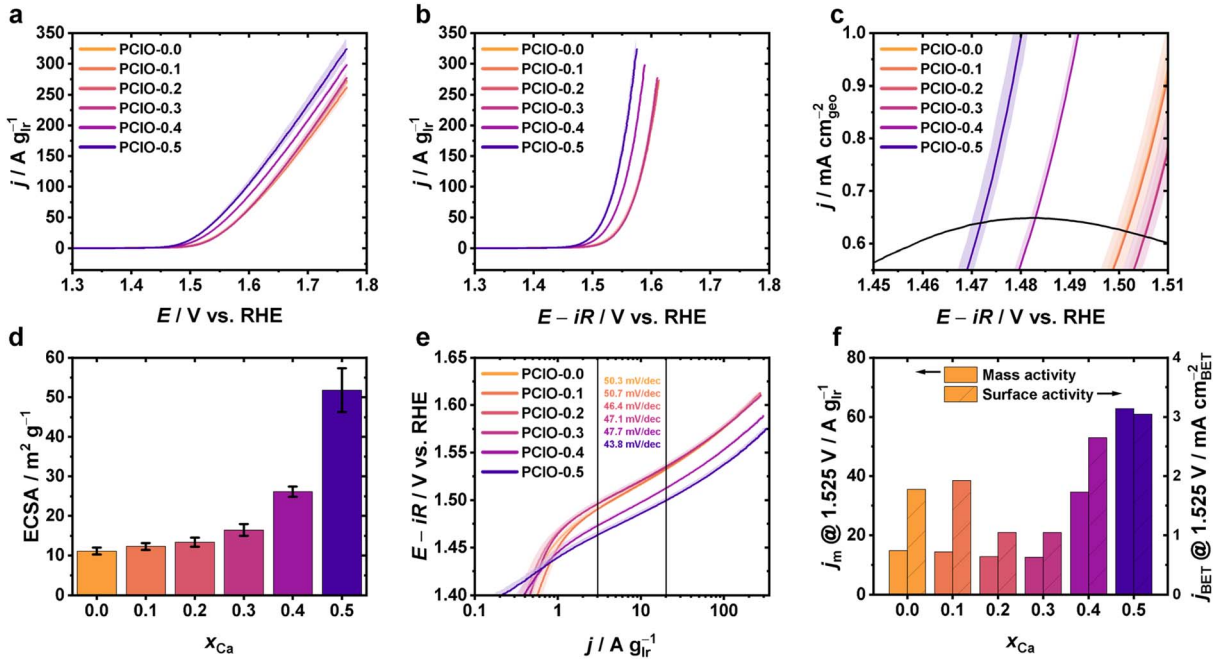


Fig. 4 Results from RDE measurement: (a) mass activity plots of the PCIO materials. The lines represent the average over three measurements, the standard deviation is given as the shaded area around the line; (b) activity plots compensated by the solution resistance, (c) onset potential determination as the potential when reaching ten times the current of the background (black line) (d) electrochemically active surface areas determined from CV measurement in non-faradaic region, (e) Tafel analysis and Tafel slopes, (f) mass activity and surface activity at 1.525 V *vs.* RHE (compensated by *iR*).

if there is also a rise in the intrinsic activity, the current densities at 1.525 V *vs.* RHE, compensated by *iR* and normalized on the mass of iridium (mass activity) as well as the BET surface of the catalysts (surface activity), an analysis similar to that done by Lebedev *et al.*, is shown in Fig. 4f.[6] Both activity measures seem to follow a similar trend, as the activities are first slightly decreasing going from $x = 0.1$ to $x = 0.3$, before they rise again, showing the highest values of 34.6 A $g_{Ir}^{-1}$ and 62.7 A $g_{Ir}^{-1}$ (2.65 mA $cm_{BET}^{-2}$ and 3.04 mA $cm_{BET}^{-2}$) with PCIO-0.4 and PCIO-0.5, respectively. Overall, the Ca-doping positively impacts several OER activity measures, most pronounced in the case of high doping levels (PCIO-0.4 and PCIO-0.5). Probably the most important improvement being the decrease of onset potential and increase in mass activity of the catalysts, making them more efficient than the undoped base compound $Pr_2Ir_2O_7$. The consistent enhancement in both mass- and BET-normalized activities in calcium-rich PCIOs ($x = 0.4$ and $x = 0.5$) indicates that the improvement arises not only from increased surface area, but from the intrinsic doping effects observed in the XPS analysis, which have been shown to enhance the catalytic activity of the material by favoring the LOM over the AEM.[17,18] In the case of PCIO-0.5 the XRD analysis showed some minor impurity phases, which could, at least to a certain extent, influence the activity of the material, *e.g.* by interfacial strain.[31] However, the SEM analysis revealed that the impurity particles are much smoother and several orders of magnitude larger than the PCIO particles, which is also expected from the sharper reflexes in the XRD. Therefore, only a negligible fraction of the catalyst powders surface should be assigned to those impurities and the interfacial area might be limited. Therefore, the activity of the material should almost solely originate from the PCIO fraction and its increase in oxygen vacancies/hydroxyl species on the surface.

In order to experimentally explore the influence of the calcium-doping on the stability of the catalysts, samples were taken from the electrolyte in the RDE cell after the measurements had finished and analyzed regarding the mass of dissolved iridium. While with the base material PCIO-0.0 213.5 ng are dissolved during the RDE measurements, this value is reduced by more than 50% when using PCIO-0.5, where a value of 97.4 ng is reached. For better comparison, the amount of dissolved iridium was determined with respect to the total mass of iridium drop-casted onto the RDE. As becomes clear from Fig. 5a the PCIO materials become more stable with increasing calcium content. Overall, regardless of the PCIO material used, less than 1% of the iridium drop-casted onto the RDE dissolves, and by this more than 99% remain intact. To get a better view on the catalysts' efficiency, the so-called stability number (*S*-number), initially introduced by Geiger *et al.*, was determined for each PCIO material.[23] The *S*-number was defined as the ratio between amount of oxygen evolved and amount of iridium dissolved, resulting in a measure that combines activity and stability of a catalyst material.[23] The higher its *S*-number the more efficient is a catalyst since more oxygen is evolved per precious metal atom dissolved.[23] The amount of evolved oxygen was determined from the total charge transferred during the CV measurements and the galvanostatic hold at 10 mA $cm_{geo}^{-2}$ assuming 100% faradaic efficiency. The detailed calculation is

 

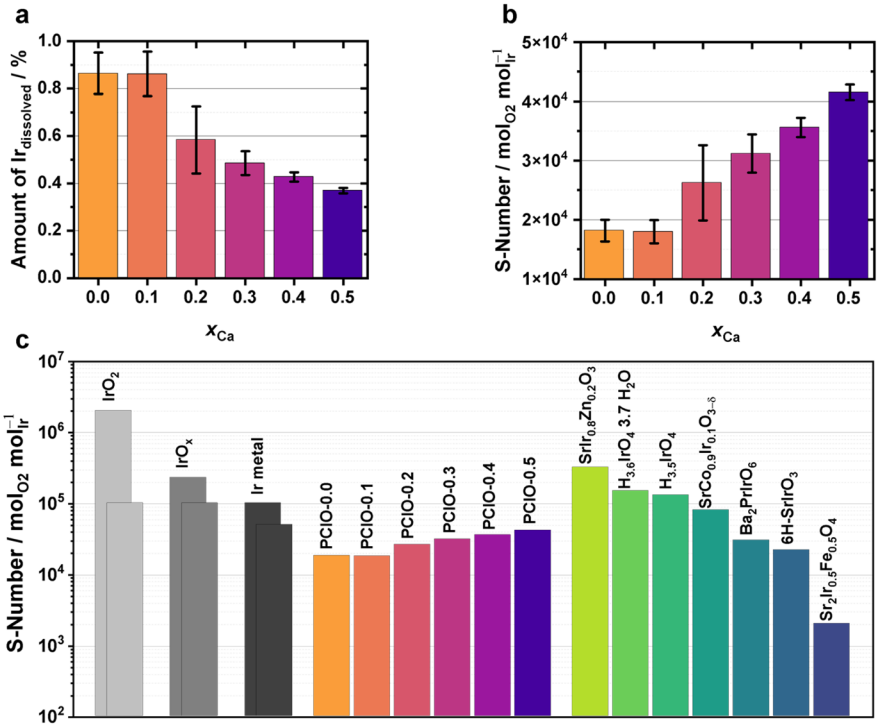


Fig. 5 Mass of iridium dissolved during the RDE measurements determined by ICP-MS: (a) amount of iridium dissolved with respect to the mass of iridium drop-casted onto the RDE disk, (b) stability number (*S*-number) determined as the fraction of oxygen evolved (sum of charge transferred during CV and the 10 mA $cm^{-2}$ holds and assuming 100% faradaic efficiency) *versus* the amount of iridium dissolved during the RDE measurement, (c) *S*-numbers of the PCIOs of this work set into context of electrocatalysts from Geiger *et al.* ($IrO_2$ left, $IrO_x$ right, Ir metal left and $Ba_2PrIrO_6$),[23] Chen *et al.* ($IrO_2$ right, Ir metal right and $SrCo_{0.9}Ir_{0.1}O_{3-\delta}$),[32] Edgington *et al.* ($IrO_x$ left and $SrIr_{0.8}Zn_{0.2}O_3$)[33] and Zhang *et al.* ($H_{3.6}IrO_4 \cdot 3.7H_2O$, $H_{3.5}IrO_4$, 6H-$SrIrO_3$ and $Sr_2Ir_{0.5}Fe_{0.5}O_4$).[34]

shown in the SI. Fig. 5b shows the obtained *S*-numbers for the six PCIO materials. There is almost no difference in the *S*-numbers of PCIO-0.0 ($1.81 \times 10^4$) and PCIO-0.1 ($1.80 \times 10^4$). For the higher calcium contents, the *S*-number gradually increases making the materials with high calcium content the most efficient OER catalysts of the series. The highly doped materials evolve almost twice (PCIO-0.4) or more than twice (PCIO-0.5) the amount of oxygen per dissolved iridium atom, with the *S*-numbers being $3.56 \times 10^4$ and $4.15 \times 10^4$, respectively. To the best of our knowledge, there are currently no *S*-number values for pyrochlore iridates published. To nevertheless put this values into a better context, the *S*-numbers of the PCIOs are plotted together with *S*-numbers of several OER catalysts (mostly iridium oxides and perovskites) from literature in Fig. 5c.[23,32–34] Since there is some variation in the *S*-numbers of iridium metal and iridium oxides in literature, we chose to depict two bars for these materials, respectively.[23,32,33] All PCIOs exhibit higher *S*-numbers than $Sr_2Ir_{0.5}Fe_{0.5}O_4$, one of the materials reported by Zhang *et al.*[34] With the calcium-doping increasing, the *S*-numbers of the PCIOs with $x \geq 0.2$ also surpass the *S*-number of 6H-$SrIrO_3$ while the PCIOs with $x \geq 0.3$ even surpass that of $Ba_2PrIrO_6$.[23,34] Still, the very high *S*-numbers of above $10^5$ $mol_{O_2}$ $mol_{Ir}^{-1}$ reached by iridium metal, the iridium oxides $IrO_2/IrO_x$ and some of the perovskite materials are not achieved with the PCIO materials, yet.[23,32–34] However, there are several studies showing that the *S*-number tends to improve over longer time of operation, due to the initially high dissolution rate of the catalyst slowing down in the course of the experiment.[23,32,35] For example, Chen *et al.* found *S*-numbers of $\sim 1 \times 10^3$ and $\sim 7 \times 10^3$ for $SrCo_{0.9}Ir_{0.1}O_{3-\delta}$ and Ir metal after 1 h of operation, which increased to $\sim 8 \times 10^4$ and $\sim 5 \times 10^4$ after 3 h of operation, respectively.[32] Furthermore, the *S*-number has been shown to be strongly influenced by the ionomer content in the catalyst layer.[36] It is to be noted that the measurement conditions (*e.g.* duration, cycling *vs.* current hold) and the ionomer contents were not exactly the same for the studies compared in Fig. 5c. However, all measurements compared where performed in an RDE setup or a setup comparable to an RDE. No *S*-numbers from GDE or MEA setups were compared, since the results would significantly vary. As was previously shown by Knöppel *et al.* *S*-numbers from MEA measurements tend to be several orders of magnitude greater than from aqueous model system measurements like ours.[36] The conditions under which the *S*-numbers shown in Fig. 5c were determined are tabulated in the SI (Table S1).

In summary, although not yet achieving the same efficiency as previously reported materials, our systematic doping study demonstrates the importance of testing materials with a broad degree of doping. While low calcium contents showed little to no influence on the activity/stability characteristics of the materials, we could significantly increase the efficiency by applying doping levels of $x = 0.4$ and $x = 0.5$, the later showing

a more than doubled *S*-number compared to the undoped variant. In our understanding, the increased activity and stability of the highly doped materials can partially, but not solely, be justified with the increase in surface area, since the two materials still show the highest surface activities of the series. Hence, we suggest, that a similar phenomenon as already described for related materials in the literature takes place: the introduction of lower valency $Ca^{2+}$ might increase the concentration of oxygen vacancies and/or surface hydroxyls and lead to higher covalency of the Ir–O bonds, promoting the LOM mechanism.[13–21,26–30] The present work focused on experimentally accessible descriptors and the derived results provide a consistent basis for the interpretation of activity and stability trends throughout the series of calcium-doped pyrochlore iridates. Complementary approaches such as comprehensive density functional theory (DFT) calculations, including electronic structure and detailed OER activity prediction, as well as characterization after OER, particularly after extended operation, could further deepen the mechanistic interpretation of the conclusions drawn within this work.

## Conclusions

We successfully demonstrated the hydrothermal synthesis of $Pr_{2-x}Ca_xIr_2O_{7-\delta}$ materials with six different calcium-doping degrees between $x = 0.0$ and 0.5 (labeled PCIO-*x*). Up to a doping content of $x = 0.4$ we obtained phase pure materials crystallizing in the pyrochlore structure. With $x = 0.5$ we examined a second phase consisting of $IrO_2$ and some minor impurities. XRF confirmed the composition of the materials as measured weight percentages of calcium, iridium and praseodymium followed the trend expected from the theoretical composition. From XRD refinement we found, that the lattice parameter slightly decreases with increasing calcium-content, due to the slight ionic radii difference between $Pr^{3+}$ and $Ca^{2+}$. Furthermore, Scherrer analysis revealed that the crystallite size of the PCIOs decreased when the calcium content is increased. This finding is backed the BET analysis and SEM images, where increasing specific surface areas and decreasing particles sizes were observed going from $x = 0.0$ to $x = 0.5$. For the first time, we then investigated the PCIO materials' activity for the OER in acidic environment. Our study shows, that the partial exchange of $Pr^{3+}$ with $Ca^{2+}$ led to improved mass activities, being exceptionally dominant with $x \geq 0.4$. XPS analysis of the O 1s region revealed, that the calcium-doping linearly increases the oxygen vacancy/surface hydroxyl concentration as an effect of charge compensation. In agreement with the findings from the specific surface area and particle size analysis, we found increased ECSAs as the calcium content increases. Finally, we probed the catalysts' stability by ICP-MS and found, that the amount of iridium dissolving during cycling and chronopotentiometry decreases with increased doping degree, indicating higher stability. By determining the *S*-number from the transferred charge and the amount of dissolved iridium, we discovered a gradually increasing efficiency of our catalyst materials, even surpassing that of some perovskite materials reported in recent literature. Within the series the Ca doping increased the *S*-number by up to more than 100%. This presents the first study were the influence of systematic doping of pyrochlore iridates on the *S*-number was investigated. In summary, we showed, that the partial exchange of $A^{3+}$ with $Ca^{2+}$ in $A_2Ir_2O_7$ pyrochlore materials represents a valid option for improving their activity and stability. Furthermore, this study shows, that the most significant advancements are only achieved with high doping levels. With this, we broaden the scope for future studies and we emphasize to exploit the limits of heterometal doping and their impact on the *S*-number in future materials and other classes of catalyst materials. Future directions, to further deepen the mechanistic interpretation of the experimentally established trends presented within this work could be complementary DFT-calculations as well as post-OER characterizations after extensive OER operation.

## Author contributions

Felix Kerner: writing – original draft, investigation, methodology, formal analysis, visualization, data curation, funding acquisition. Kohei Miyazaki: writing – review and editing, conceptualization, resources, supervision, funding acquisition. Daniel Schröder: writing – review and editing, resources, supervision, funding acquisition.

## Conflicts of interest

There are no conflicts to declare.

## Data availability

The data supporting the findings of this study are available within the article and/or the supplementary information (SI). Supplementary information: XRF analysis, BET analysis, SEM images, SEM-EDX images, XPS of Ir 4f region, ECSA determination, *S*-number determination. Raw data are available from the corresponding author upon reasonable request. See DOI: https://doi.org/10.1039/d5ta08986g.

## Acknowledgements

The authors acknowledge funding by the Federal Ministry of Research, Technology and Space (BMFTR) within the project 01DR22006A (DECoH). This work was supported by a fellowship of the German Academic Exchange Service (DAAD). The authors acknowledge Valerie N. Mohni for conducting the SEM measurements.

## References

1 M. Chatenet, B. G. Pollet, D. R. Dekel, F. Dionigi, J. Deseure, P. Millet, R. D. Braatz, M. Z. Bazant, M. Eikerling, I. Staffell, P. Balcombe, Y. Shao-Horn and H. Schäfer, *Chem. Soc. Rev.*, 2022, **51**, 4583–4762.
2 C. Van Pham, D. Escalera-López, K. Mayrhofer, S. Cherevko and S. Thiele, *Adv. Energy Mater.*, 2021, **11**, 2101998.

 

3 N. T. T. Thao, J. U. Jang, A. K. Nayak and H. Han, *Small Sci.*, 2024, **4**, 2300109.
4 C. Minke, M. Suermann, B. Bensmann and R. Hanke-Rauschenbach, *Int. J. Hydrogen Energy*, 2021, **46**, 23581–23590.
5 P. C. Shih, J. Kim, C. J. Sun and H. Yang, *ACS Appl. Energy Mater.*, 2018, **1**, 3992–3998.
6 D. Lebedev, M. Povia, K. Waltar, P. M. Abdala, I. E. Castelli, E. Fabbri, M. V. Blanco, A. Fedorov, C. Copéret, N. Marzari and T. J. Schmidt, *Chem. Mater.*, 2017, **29**, 5182–5191.
7 L. C. Seitz, C. F. Dickens, K. Nishio, Y. Hikita, J. Montoya, A. Doyle, C. Kirk, A. Vojvodic, H. Y. Hwang, J. K. Norskov and T. F. Jaramillo, *Science*, 2016, **353**, 1011–1014.
8 O. Diaz-Morales, S. Raaijman, R. Kortlever, P. J. Kooyman, T. Wezendonk, J. Gascon, W. T. Fu and M. T. M. Koper, *Nat. Commun.*, 2016, **7**, 12363.
9 P. Gayen, S. Saha and V. Ramani, *Acc. Chem. Res.*, 2022, **55**, 2191–2200.
10 C. W. Song, H. Suh, J. Bak, H. Bin Bae and S. Y. Chung, *Chem*, 2019, **5**, 3243–3259.
11 J. Kim, P. C. Shih, K. C. Tsao, Y. T. Pan, X. Yin, C. J. Sun and H. Yang, *J. Am. Chem. Soc.*, 2017, **139**, 12076–12083.
12 C. Shang, C. Cao, D. Yu, Y. Yan, Y. Lin, H. Li, T. Zheng, X. Yan, W. Yu, S. Zhou and J. Zeng, *Adv. Mater.*, 2019, **31**, 1805104.
13 Q. Feng, Q. Wang, Z. Zhang, Y. Xiong, H. Li, Y. Yao, X. Z. Yuan, M. C. Williams, M. Gu, H. Chen, H. Li and H. Wang, *Appl. Catal., B*, 2019, **244**, 494–501.
14 Q. Feng, Z. Zhang, H. Huang, K. Yao, J. Fan, L. Zeng, M. C. Williams, H. Li and H. Wang, *Chem. Eng. J.*, 2020, **395**, 124428.
15 Q. Feng, Z. Zhao, X. Z. Yuan, H. Li and H. Wang, *Appl. Catal., B*, 2020, **260**, 118176.
16 Q. Feng, J. Zou, Y. Wang, Z. Zhao, M. C. Williams, H. Li and H. Wang, *ACS Appl. Mater. Interfaces*, 2020, **12**, 4520–4530.
17 D. A. Kuznetsov, M. A. Naeem, P. V. Kumar, P. M. Abdala, A. Fedorov and C. R. Müller, *J. Am. Chem. Soc.*, 2020, **142**, 7883–7888.
18 P. Wang, Q. Cheng, C. Mao, W. Su, L. Yang, G. Wang, L. Zou, Y. Shi, C. Yan, Z. Zou and H. Yang, *J. Power Sources*, 2021, **502**, 229903.
19 R. Yang, Q. Hao, J. Zhao, C. Lei, S. Xue, F. Miao, W. Tang, Q. Huang, J. Wang and Y. Wu, *J. Alloys Compd.*, 2024, **986**, 174072.
20 L. Zhu, C. Ma, Z. Wang, X. Gong, L. Cao and J. Yang, *Appl. Surf. Sci.*, 2022, **576**, 151840.
21 J. Shan, Y. Zheng, B. Shi, K. Davey and S. Z. Qiao, *ACS Energy Lett.*, 2019, **4**, 2719–2730.
22 E. M. S. Converse, PhD thesis, Oregon State University, 2020.
23 S. Geiger, O. Kasian, M. Ledendecker, E. Pizzutilo, A. M. Mingers, W. T. Fu, O. Diaz-morales, Z. Li, T. Oellers, L. Fruchter, A. Ludwig, K. J. J. Mayrhofer, M. T. M. Koper and S. Cherevko, *Nat. Catal.*, 2018, **1**, 508–515.
24 Y. Wu, W. Sun, Z. Zhou, W. Q. Zaman, M. Tariq, L. Cao and J. Yang, *ACS Omega*, 2018, **3**, 2902–2908.
25 D. R. Lide, S. R. Data, E. A. Board, G. Baysinger, S. Chemistry, C. E. Library, L. I. Berger, R. N. Goldberg, B. Division, H. V Kehiaian, K. Kuchitsu, G. Rosenblatt, D. L. Roth and D. Zwillinger, *CRC Handbook of Chemistry and Physics*, 2004.
26 H. Miao, Z. Wang, Q. Wang, S. Sun, Y. Xue, F. Wang, J. Zhao, Z. Liu and J. Yuan, *Energy*, 2018, **154**, 561–570.
27 J. Zhu, H. Li, L. Zhong, P. Xiao, X. Xu, X. Yang, Z. Zhao and J. Li, *ACS Catal.*, 2014, **4**, 2917–2940.
28 J. T. Mefford, X. Rong, A. M. Abakumov, W. G. Hardin, S. Dai, A. M. Kolpak, K. P. Johnston and K. J. Stevenson, *Nat. Commun.*, 2016, **7**, 11053.
29 L. Yang, H. Chen, L. Shi, X. Li, X. Chu, W. Chen, N. Li and X. Zou, *ACS Appl. Mater. Interfaces*, 2019, **11**, 42006–42013.
30 T. Reier, Z. Pawolek, S. Cherevko, M. Bruns, T. Jones, D. Teschner, S. Selve, A. Bergmann, H. N. Nong, R. Schlögl, K. J. J. Mayrhofer and P. Strasser, *J. Am. Chem. Soc.*, 2015, **137**, 13031–13040.
31 T. Yang, Y. Yan, R. Liu, K. Huang, R. Xu, J. Chen, J. Tu, S. Liu, L. Kang, Z. Wang, J. Cao and J. Qi, *Nano Lett.*, 2025, **25**, 7707–7715.
32 Y. Chen, H. Li, J. Wang, Y. Du, S. Xi, Y. Sun, M. Sherburne, J. W. Ager, A. C. Fisher and Z. J. Xu, *Nat. Commun.*, 2019, **10**, 572.
33 J. Edgington, A. Deberghes and L. C. Seitz, *ACS Appl. Energy Mater.*, 2022, **5**, 12206–12218.
34 R. Zhang, P. E. Pearce, V. Pimenta, J. Cabana, H. Li, D. Alves Dalla Corte, A. M. Abakumov, G. Rousse, D. Giaume, M. Deschamps and A. Grimaud, *Chem. Mater.*, 2020, **32**, 3499–3509.
35 M. A. Hubert, A. M. Patel, A. Gallo, Y. Liu, E. Valle, M. Ben-Naim, J. Sanchez, D. Sokaras, R. Sinclair, J. K. Nørskov, L. A. King, M. Bajdich and T. F. Jaramillo, *ACS Catal.*, 2020, **10**, 12182–12196.
36 J. Knöppel, M. Möckl, D. Escalera-López, K. Stojanovski, M. Bierling, T. Böhm, S. Thiele, M. Rzepka and S. Cherevko, *Nat. Commun.*, 2021, **12**, 2231.